

Correlation-induced phase shifts and time delays in resonance enhanced high harmonic generation from Cr^+

Yoad Aharon,¹ Adi Pick,¹ Amir Hen,¹ Gilad Marcus,^{1,*} and Ofer Neufeld^{2,†}

¹*Institute of Applied Physics, Hebrew University of Jerusalem, Jerusalem 9190401, Israel*

²*Technion Israel Institute of Technology,
Faculty of Chemistry, Haifa 3200003, Israel*

(Dated: July 2, 2025)

arXiv:2507.00526v1 [physics.atom-ph] 1 Jul 2025

Abstract

We investigate resonance-enhanced high harmonic generation (rHHG) in Cr^+ by comparing a 1D shape-resonant model, time-dependent density functional theory (TDDFT), and independent particle approximation (IPA) simulations. Previous studies linked rHHG to the $3p \rightarrow 3d$ giant resonance, suggesting a modified four-step model where recolliding electrons are first captured in the autoionizing state before recombining into the ground state, potentially leading to an emission delay associated with the resonance lifetime. While both the 1D-model and TDDFT reproduce experimental spectra, TDDFT reveals that rHHG counterintuitively originates from spin-down $3p$ states, while spin-up $3d$ electrons negligibly contribute. The IPA fails to reproduce rHHG, highlighting the significance of electron correlations. Furthermore, TDDFT revealed a correlation-induced ~ 480 attosecond time delay, accompanied by a strong phase shift across the resonance, potentially explaining earlier RABBIT measurements. Our work sheds light on long-standing open questions in rHHG and should advance novel ultrafast spectroscopies of electron correlations and resonances.

INTRODUCTION

High-harmonic generation (HHG) is a fundamental process in strong-field physics that enables the generation of coherent extreme ultraviolet (XUV) and soft X-ray radiation[1–5]. It presents a powerful tool for probing ultrafast electron dynamics and structural properties of matter across phases [6–21]. In gases, HHG is commonly well described by a semi-classical three-step model [22, 23] whereby an electron: (i) tunnel ionizes due to intense laser irradiation, (ii) is accelerated by the laser in the continuum, and (iii) recombines with the parent ion, emitting a high-energy photon. The coherence of the electronic wave function throughout this process is key towards utilizing HHG for ultrafast spectroscopy, as has been demonstrated for charge migration[16, 24], molecular symmetry and orientation [25–33], and more.

The typical HHG spectrum consists of odd harmonics with nearly uniform intensity, forming a characteristic plateau. This uniformity is observed across material systems and arises from the periodicity of the generation mechanism. Consequently, the electronic structure of the generating medium is not directly apparent within the HHG spectrum.

One known gas-phase system that deviates from this three-step model picture is transition-metal ions. Experimentally, HHG from laser-ablated plasma is known to lead to a sharp resonance in which a single harmonic order is significantly enhanced [34–36]. Resonant HHG (rHHG) has been established to originate microscopically at the single atom level, with macroscopic effects playing a negligible role [36]. Here, the energy of the enhanced harmonic photon aligns with a transition to an existing autoionization state (AIS) in the cation, related to the $3p \rightarrow 3d$ giant resonance (which is a dominant feature in absorption spectra of transition metal ions). This phenomenon involves the excitation of a $3p$ core electron to an unoccupied $3d$ subshell [37–39]. Its significant strength arises from large electric dipole matrix elements between the $3p$ and $3d$ orbitals, which results from their close spatial overlap. This overlap is strong because the occupied $3d$ subshell wave function is located inside an effective potential barrier, while higher energy $3d$ orbitals are pushed out due to a centrifugal barrier component of the effective radial potential. Following excitation, the resulting highly excited state (e.g., $3p^5 3d^{n+1}$) is unstable and rapidly decays through autoionization into continuum states, typically filling the $3p$ hole and emitting an outer electron (e.g., $3p^6 3d^{n-1} + \epsilon l$). This decay mechanism gives the resonance a large width. The interaction and interference between this indirect autoionization channel and direct photoionization channels (such as $d \rightarrow \epsilon f$) results in the characteristic asymmetric Fano-type line shapes observed in the absorption and photoionization spectra. For Cr^+ , the ground state configuration is $3p^6 3d^5(^6S)$ in terms of total angular momentum notation (LS coupling). The dominant excitation is still the $3p \rightarrow 3d$ transition, i.e. $\text{Cr}^+ 3p^6 3d^5(^6S) + \gamma \rightarrow \text{Cr}^+ 3p^5(^2P)3d^6(^5D)(^6P)$ followed by autoionization into $\text{Cr}^{2+} 3p^6 3d^4(^5D) + \epsilon l$ with $l = 3$ being the dominant channel [37–39].

In HHG conditions these light-induced transitions are further complexified because electrons can absorb multiple photons simultaneously, allowing multiphoton transitions as well as tunneling to occur. An extended semi-classical 4-step model was suggested to explain rHHG. Essentially, the normal recombination step in the 3-step model is replaced by a capture process in the AIS, followed by a resonant single-photon transition to the ground-state, emitting an enhanced harmonic photon. This can be considered the reverse process of autoionization, in which an energetic photon is first absorbed in the atom and promotes a $3p$ electron to the $3d$ level, followed by the ejection of an electron to the continuum while filling the $3p$ hole.

Numerical simulations for rHHG divide into two categories: (i) model simulations where the AIS is approximated by a shape resonance in a barrier-well potential system, forming a metastable state (MS) [40–42]. This model correctly reproduces measured enhancements, but does so by fitting the transition energy to experimental observations. With this approach, it remains unclear to what extent the single-electron approximation captures the full dynamics of rHHG, and especially, if there is any time-delay or phase shift incurred to the resonant photon due to passage through the AIS (with reference to RABBIT experiments that suggested a strong phase shift within the resonant harmonic [43]). Approach (ii) is to perform *ab-initio* simulations of rHHG using either time-dependent density functional theory (TDDFT) [44, 45], or multi-configuration time-dependent approaches [46, 47]. These schemes lead to spectra in agreement with experiments without the need of external parameters, but are more difficult to analyze and extract the physical mechanism. Still, with *ab-initio* schemes it was established that in some systems correlations play a dominant role in enabling resonant emission [44], and that deeper orbitals can often play a crucial role in dynamics [46]. What remains unclear is how these effects transpire, and how they depend on the electronic spin in magnetic ions such as Cr^+ . In particular, the phase and time delay of rHHG has not yet been explored or compared with simpler models.

Here we perform an extensive theoretical analysis of rHHG from the magnetic Cr^+ system. We employ three complementary levels of theory: (i) a simple shape-resonant model, (ii) *ab-initio* spin-TDDFT simulations, and (iii) simulations on par with the spin-TDDFT system but where correlations between electrons are artificially frozen, denoted as the independent particle approximation (IPA). This comparison allows us to pin-point the exact mechanisms of rHHG - deeper $3p$ orbitals that generally have a much higher ionization potential and are not expected to contribute. We show that the role of electron correlations is to allow $3p$ electrons to transition into empty $3d$ bands, from which recombination through the AIS is possible. This transition does not occur in uncorrelated theories, and further incurs a time-delay and phase shift onto the rHHG emission, suggesting correlated corrections to the 4-step model. Importantly, we find that this transition is only facilitated by spin-down electrons that can pass through the empty d -bands. Our results shed light onto fundamental rHHG physical and could lead to HHG-spectroscopy of attosecond correlated multi-electron systems.

RESULTS

As a first step, we calculate HHG spectrum and corresponding time-frequency plots from the 1D model under typical experimental conditions. The results in Fig. 1 show a good match to known experimental rHHG spectra from Cr^+ . We begin by examining the behavior of H29 for different MS lifetimes (Fig. 1 b). Following ref. [48], the lifetime is calculated from the imaginary part of the energy, $\tau = -\frac{\hbar}{2\text{Im}[E_{res}]}$. We plot the harmonic spectra normalized to the intensity of H27, and use this to quantify the enhancement factor of the resonant H29, defined as $\frac{I_{29}}{I_{27}}$. While the overall harmonic yield decreases with increasing MS lifetime (see SI), the enhancement factor increases. This decrease in yield is consistent with a recollision-based model, since the increase in lifetime is achieved by widening the barrier, which decreases the tunneling rate. To further investigate this interpretation, we repeated the simulation while gradually extending the PML inwards (see the Computational Methods section below and SI) from the box boundary toward its center. As the PML approached the region associated with the semiclassical long trajectories, these trajectories progressively disappeared from the time-frequency plots. In contrast, the short trajectories remained unaffected as they do not extend as far from the nucleus as the long trajectories (see SI). The harmonic spectra was also affected by the advance of the PML into the simulation domain, showing a decrease in yield, beginning with the highest harmonic orders and progressively impacting lower ones. Crucially, the intensity of H29 also decreased. This validates that rHHG in the 1D model is a tunneling-based phenomena, as expected from the 4-step model.

The time-frequency analysis for an exemplary case is shown in Fig. 1(c). Notably, the electron trajectories calculated using the semi-classical 3-step model (see SI for details) match the simulation with high accuracy. Specifically, there is no distinguishable time delay between the emission time of the resonant H29 and that predicted by the 3-step model. We note that according to the 4-step model, H29 is emitted after the electron is captured in the AIS, therefore, some additional delay is anticipated due to the time the electron spends in the AIS. However, no significant delay is observed in our 1D simulations for varying resonance lifetimes.

Next, we employ the *ab-initio* TDDFT scheme. Figure 2 shows HHG spectra and time-frequency analysis under similar conditions to Fig. 1 separated to spin-up/down channels (Fig. 2(c,d)), and the total spin-summed response (Fig. 2(b)). While both channels con-

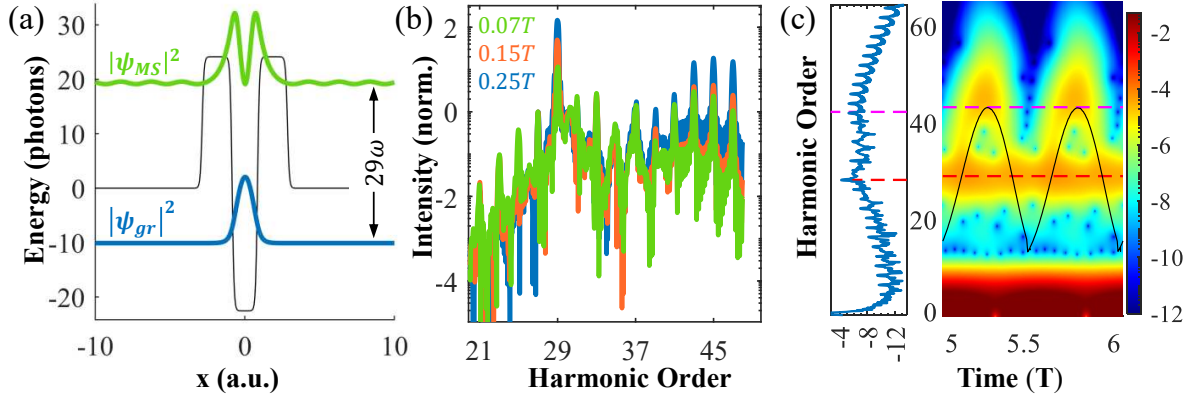


Figure 1. **rHHG from the 1D model.** (a) Potential supporting a shape resonance (MS, black). The ground state (blue) and MS (green) densities are plotted in their respective eigen-energies. The vertical axis (energy) is normalized to the driving photon energy. (b) HHG spectra for different barrier widths/MS lifetimes. Curves are normalized to the 27th harmonic. The enhancement coefficient increases with the MS lifetime. (c) (Right) Gabor transform of HHG emission for an MS lifetime of $0.17T$ (T is the period of the driving laser). Red, purple, and black curves indicate the resonant harmonic energy, the semiclassical cutoff energy, and semiclassical emission times (trajectories), respectively. (Left) Corresponding spectrum. The enhancement of the resonant harmonic H29 is evident in both the spectrum and the Gabor transform. The harmonic emission times are in strong agreement with the semiclassical model.

tribute to the resonance emission, the spin-down channel response is about an order of magnitude larger than the spin-up channel, and in fact dominates rHHG. This is counter-intuitive if considering the typical physical mechanism of atomic HHG and the energy level diagram in Fig. 2(b) - the spin-up channel includes initially occupied $3d$ states that have a much smaller ionization potential compared to the $3p$ levels. *A-priori*, this should make their tunnel ionization and subsequent recombination exponentially more efficient. However, the fact that $3p$ spin-down states dominate the resonant response indicates that they become intimately linked to the AIS through interaction with the laser.

Another surprising feature can be seen in the time-frequency plots in Fig. 2 that is overlaid with the corresponding semi-classical three-step model trajectories. First, we notice that the HHG emission time in the spin-up channel largely follows the semi-classical trajectories with ionization potential matching the $3d$ levels. This is expected since the $3d$ spin-up sub-shell is initially occupied and its ionization energy is much lower than the ionization

energy of the $3p$ electrons (which are seen to contribute negligibly at higher energies). The most striking feature is that the HHG emission from the spin-down channel also largely follows the classical trajectories initiated from $3d$ electrons, even though the $3d$ states are not initially occupied by spin-down electrons. This is a direct indication that rHHG is involved and induces a $3p \rightarrow 3d$ transition, while this channel is blocked for the $3p$ spin-up electrons due to the $3d$ spin-up bands being already fully occupied.

Another prominent feature of the *ab-initio* spectra is that the timing of the resonance emission is shifted from the expected long/short trajectories. From Fig. 2(c), the resonant emission time in the spin-up channel follows roughly the typical long/short HHG semi-classical trajectories (as in the 1D model). However, in the more dominant spin-down channel the resonance emission is delayed by $\sim 0.18T \approx 480$ attoseconds. This result contradicts that from the 1D single active electron model, suggesting electron interaction and spin-selective mechanism by which AIS resonances enhance HHG. Interestingly, the resonant emission yield builds up as the simulation progresses, while this build-up is absent in the non-resonant harmonics and in the spin-up channel, suggesting population of the AIS is playing a key role. A possible mechanism for this is given by the 4-step model in which a $3d$ electron first tunnels out ($\text{Cr}^+ 3p^6 3d^5(^6S) \rightarrow \text{Cr}^{2+} 3p^6 3d^4(^5D) + eI$), gains kinetic energy in the laser field, and re-collides with Cr^{+2} to excite a partial $3p$ spin-down electron wavepacket into the $\text{Cr}^+ 3p^5(^2P) 3d^6(^5D)(^6P)$ AIS, forming a superposition of AIS and ground state. This superposition has a time dependent dipole moment that oscillates at the frequency of H29.

To further explore this conjecture, we repeat our simulations but invoking the IPA, i.e. freezing electronic interactions altogether. The results are shown in fig. 3 for both spin channels and the total emission, and reflect a prominent effect - upon freezing correlations the resonance enhancement is completely suppressed. Similar results were recently shown in another system[44]. Here however, the spin-up channel HHG response remains largely similar with/without the IPA, while the spin-down HHG response is substantially suppressed and is the source of the disappearance of rHHG in the absence of correlations. Notably, the emission from the spin-down electrons no longer follows the semi-classical trajectories of the $3d$ electrons, proving that the spin-down $3p \rightarrow 3d$ transition is facilitated by dynamical electron correlations even in the tunneling regime. We further note that while the resonance emission line still exists in the IPA spin-down channel, it is orders of magnitude weaker, and has phase shifted and is now aligned with the maximum of the electric field, similar

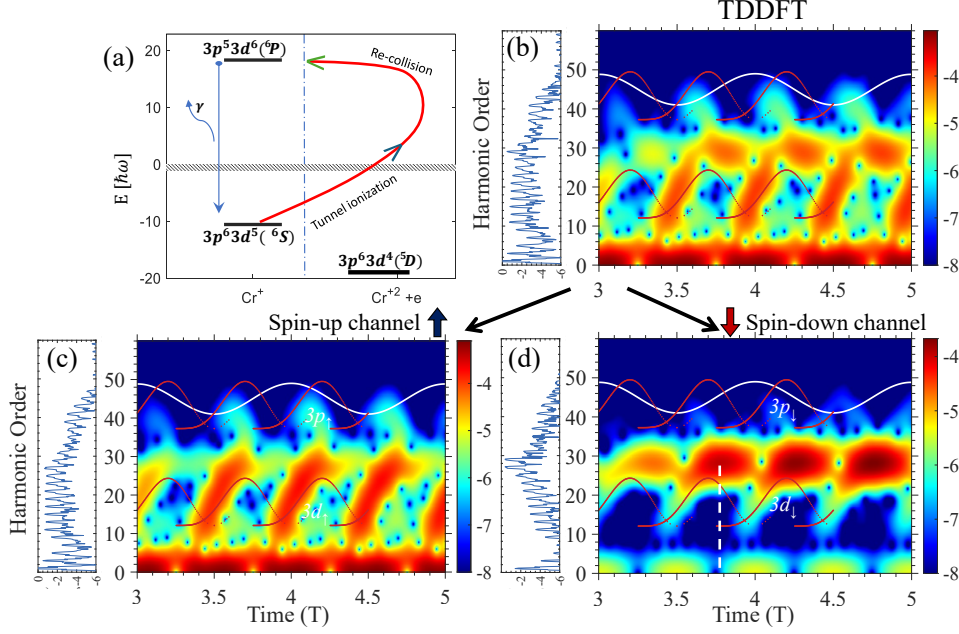


Figure 2. **rHHG with TDDFT.** (a) Energy level configuration in Cr^+ . (b) (Right) Gabor transform of total calculated HHG emission. (Left) Corresponding HHG spectrum. Top and bottom red curves denote the emission time and energy according to the classical trajectories of the 3-step model (low energy curves associated to $3d$ electrons and high energy curves are associated to $3p$ electrons). White lines illustrate the driving field. (c) Same as (a) but for spin-up response, roughly following the semiclassical model for $3d$ electrons. (d) Same as (c) but for spin-down response, where $3p$ spin-down states dominate rHHG (see color scales in (c) and (d)), which is delayed by 250 as relative to spin-up response.

to the perturbative low-order harmonics. In that respect, even though the atomic system still support a resonant state in the absence of correlations, it does not contribute to rHHG since emission from typical HHG channels is more prominent, and the resonance emission mechanism differs from that of the correlated system.

We further note that the spin-down channel HHG emission in the IPA is very similar in nature to the emission profile obtained from the simple 1D model. Both spectra exhibit a strong dip in the lower harmonics followed by a rise that peaks at resonance. In the 1D model, this has been attributed to the decrease in the ability of the returning electron to penetrate the potential barrier [41]. The similar shape in the IPA spin-down emission, and the lack of resonance in spin-up emission, may be indicative of a shape resonance formed by the time-independent electron-electron interaction[39]. Further, the significantly lower

harmonic yield due to IPA spin-down electrons vs spin-up is also consistent with the presence of a shape-resonance, similar to the results in Fig. 1(b).

Overall, we conclude that in the IPA the $3p$ down states do not transition into $3d$ states, and the resonance is emitted by pure multi-photon transitions rather than excitation through the continuum following a separate physical mechanism compared to the correlated theory. In contrast, spin-down $3p$ electrons require electronic correlations in order to resonantly emit HHG in Cr^+ in experimental settings, following their transition into $3d$ levels, also incurring a time delay. These results are further corroborated by ab-initio simulations for the single-photon absorption and ionization cross sections (see SI), supporting our conclusions that the down spin channel is the main contributor to absorption at the resonance, which only occurs with correlations.

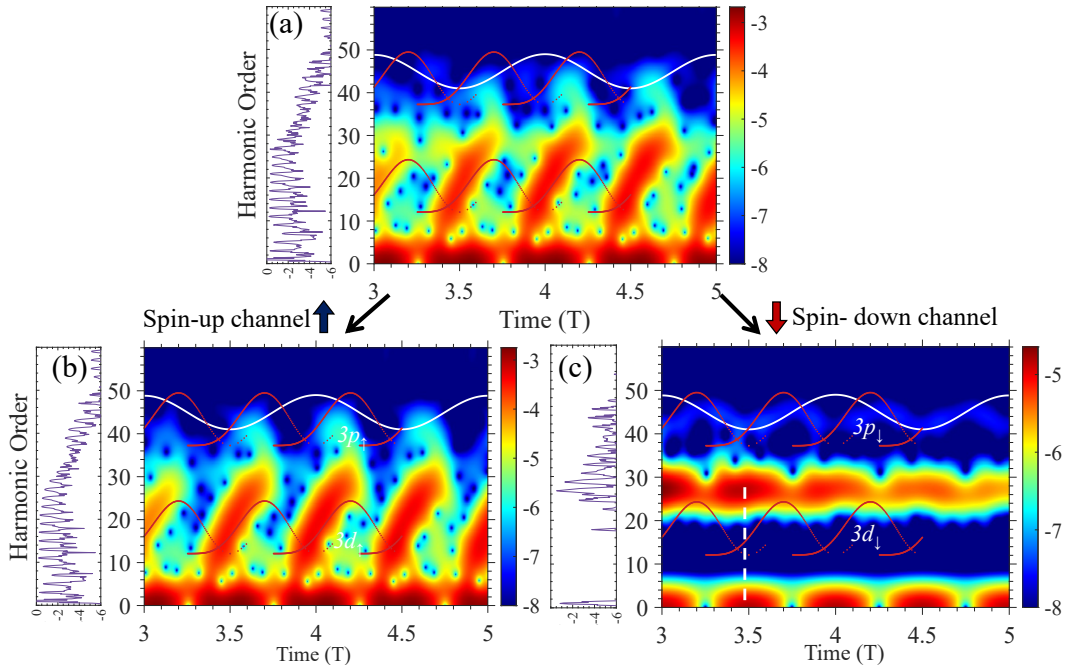


Figure 3. **rHHG within the IPA.** (a-c) Same as (b-d) in Fig.2. Note the spin-down response on resonance is in-phase with the maxima/minima of the driving field and strongly suppressed, unlike in Fig.2.

Finally, we explore the phase of the harmonics at all levels of theory with a RABBIT-like simulation (see details in the SI). From the RABBIT calculation we extract the harmonic phase across orders, as well as the RABBIT sideband (SB) visibility per order. The results presented in Fig. 4(a) show a clear conclusion - a sharp phase jump across the resonance is

induced only in the correlated theory. This shift is up to 2.3π through the resonance, and is followed by a reduction in the expected sideband visibility. A vertical shift of the IPA curve to align with the start or end of the correlated curve (dotted gray lines with dot markers) shows excellent agreement between the models, except near the resonance, highlighting the role of electron correlations in determining harmonic phases in rHHG. Note that we have found that differences in the 1D and IPA simulations can be corrected for with group velocity delay corrections (blue line in Fig. 4(a), see SI for details), which renders both theories analogous. The predicted phase jump in rHHG can potentially explain previous measurements of reduced SB visibility to either side of the resonant harmonic [43], since it suggests a sharp phase jump even within the resonant harmonic itself (the 2.3π shift occurs abruptly over 4 harmonic orders, translating roughly to 0.5π jump within the resonant harmonic).

To further test this, Fig. 4(b) presents the actual numerically-observed RABBIT SB visibility and the expected visibility due to two-source interference (taking into account the harmonic yields). The normalized visibility (observed/expected) is shown in Fig. 4(c). For both SB28 and SB30 (closest to the resonance), across all models, the expected visibility is larger than the observed visibility (with the exception of SB30 IPA spin-down channel where they are roughly equal). For both SBs, the normalized correlated visibility is drastically lower than the normalized IPA visibility (SB28 - 15.1% vs 27.1%; SB30 5.6% vs 35%). Looking at the spin-resolved components, we see similar behavior, with the most noticeable case being the spin-down component responsible for rHHG in SB30 (4% vs 103.5%). A similar but opposite difference arises between the spin-up component of SB30 (48.5% vs 4.5%), which we attribute to the extremely low harmonic signal in the IPA spin-up channel. Interestingly, the 1D single-electron model yields a normalized visibility similar to that of the spin-down component in the correlated model. This contrasts with the harmonic phase, which more closely resembles that of the IPA model. While this may seem unexpected, it is important to note that the 1D and IPA models are not equivalent. The 1D model employs a synthetic potential supporting a sharp shape resonance, which may differ from the IPA simulations, where this resonance could be less pronounced. Crucially, only the fully correlated theory accurately reproduces the correct harmonic phase near resonance, highlighting the central role of electron correlation in this regime, also sharply reducing SB visibility in correspondence with measurements[43].

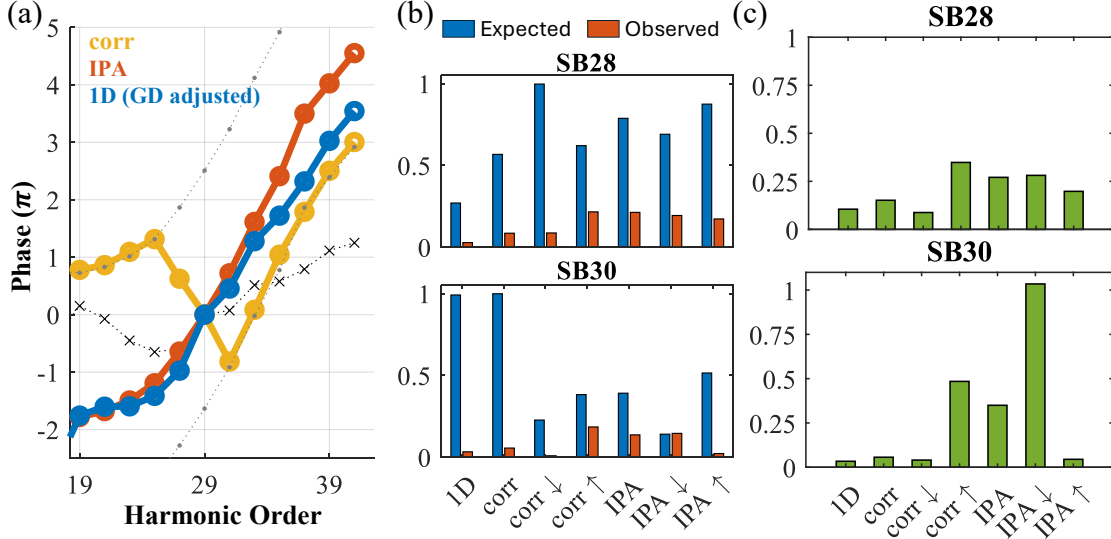


Figure 4. **rHHG phase and RABBIT analysis.** (a) Harmonic phase comparison with varying levels of theory. Yellow and orange curves denote the fully correlated and IPA simulations, respectively. The blue line denotes the group-delay-corrected 1D simulation (see text). Gray dotted lines with dot markers indicate the vertically shifted IPA results, while the gray dotted line with \times markers corresponds to the unadjusted 1D result. (b) Observed and expected SB visibility (for SB28 and SB30) for various levels of theory and spin channel contributions. (c) Normalized visibility (ratio of observed/expected) for both sidebands and various levels of theory. The correlated theory shows much reduced visibility compared to the expected value, corresponding to the strong phase jump in (a).

SUMMARY AND OUTLOOK

In summary, we theoretically explored resonance-enhanced high harmonic generation (rHHG) in Cr^+ ions by employing three complementary approaches: (i) a 1D single electron model where the resonance is modeled by a shape-resonance, (ii) *ab-initio* spin-time-dependent density functional theory (spin-TDDFT), and (iii) spin-TDDFT within the independent particle approximation (IPA) with electronic interactions artificially removed.

The 1D model successfully reproduces experimental rHHG spectra, where we showed that the mechanism for rHHG in this case is tunnel-ionization followed by re-collision (without associated time delays). TDDFT also reproduces experimental spectra, but offers a more comprehensive view into rHHG physics — We uncovered that the primary contribution to

enhancement originates from spin-down $3p$ states rather than spin-up $3d$ electrons (that intuitively should dominate due to their lower ionization potential). Strikingly, the more dominant spin-down emission is delayed by ~ 480 attoseconds compared to the spin-up $3d$ emission. These effects contrast with the 1D model and IPA simulations and point towards a mechanism involving electron interaction and spin selectivity, also aligning with the 4-step picture: A $3d$ spin-up electron tunnel ionizes and accelerates in the continuum. Subsequently, it re-collides with the parent ion, exciting a $3p$ spin-down electron (only possible through correlations), trapping both electrons in the autoionizing state. The autoionization level proceeds to coherently decay to the ground state, emitting a resonantly-enhanced photon. Lastly, we explored RABBIT simulations that investigate the harmonic phases and sideband visibility. These simulations showed a sharp phase jump ($\sim 2.3\pi$) across the resonance that occurred only in the correlated theory. Correspondingly, normalized sideband visibility near the resonance was drastically lower in the correlated theory compared to the IPA (especially for the dominant spin-down component), which might explain earlier measurements[43].

Overall, our work establishes that the resonance enhancement mechanism is physically different in the absence of correlations, and thus suggests that single electron and semi-classical models must be phase and time-delay corrected due to electronic interactions. Our work resolves several open questions in the field, and should pave way to novel ultrafast spectroscopies of electron correlations and resonances.

COMPUTATIONAL METHODS

In this study we employed several complementary theoretical descriptions of rHHG from Cr^+ . First, we implemented a 1D model scheme with a potential supporting a shape-resonance. To this end, we used a square barrier-well system, where the boundaries between the piecewise domains were rounded using a hyperbolic function $\tanh(\alpha x)$, with $\alpha = \frac{1}{8 \text{ a.u.}}$ (see Supplementary Information (SI) for details). Before applying the smoothing, the potential is defined as: $V(x) = V_w$ if $|x| \leq l_w$; V_b if $l_w < |x| \leq l_w + l_b$; 0 otherwise,

where l_w is the width of the potential well, l_b is the width of the potential barrier, V_w is depth of the potential well (a negative quantity) and V_b is the barrier height (a positive quantity).

The values of the ionization potential I_p and the MS energy E_{MS} were selected to approximately match that of Cr^+ (the model I_p is ~ 15.8 eV, while the experimental value is ~ 16.4 eV[49]). The energy levels, including I_p and E_{MS} , are computed using the method of complex-scaling [50]. The potential is plotted in Fig. 1(a). Tuning the model parameters allow to systematically control the lifetime of the MS state, e.g. by increasing the barrier width (reducing the tunneling rate), thereby increasing the lifetime, while altering the ground-state energy and wavefunction only negligibly. Within this 1D model the time-dependent Schrödinger equation (TDSE) is represented on a real-space grid where the initial state is chosen to be the s -like (symmetric) ground state, with the shape resonance residing in a p -like level, and the potential parameters are fitted to obtain a transition energy within the experimentally observed enhanced harmonic order (fundamental laser at 800 nm driving results in enhanced 29th harmonic). We used the driving field of the form:

$$E(t) = f(t) \cos(\omega t), \quad (1)$$

where $f(t)$ is an envelope function in which the amplitude ramps up following a super-sine function [51], remains constant, and then decays. The driving frequency ω is set such that H29 is in resonance with the ground-MS transition $29\omega = I_p + E_{MS}$. For the main simulation, corresponding to a MS lifetime of 0.17T, this results in $\omega = 0.0621$ [a.u.], or 734 nm. We numerically solved the TDSE in the dipole approximation and length gauge, given in atomic units by:

$$\left[i \frac{\partial}{\partial t} + \frac{1}{2} \frac{\partial^2}{\partial x^2} - V(x) - xE(t) \right] \psi(x) = 0 \quad (2)$$

where we further employed the method of perfectly-matched layers (PML) [52] to suppress reflections from the grid boundaries.

From the propagated state, $\psi(x, t)$, we obtain the dipole acceleration through Ehrenfest's theorem [53] as $a(t) = \frac{1}{i} \left\langle \left[\hat{P}, \hat{H} \right] \right\rangle$, from which the HHG spectrum is calculated using a Fourier transform: $I(\Omega) = \left| \frac{1}{\sqrt{2\pi}} \int_{-\infty}^{\infty} a(t) e^{-i\Omega t} dt \right|^2$. Time domain information is obtained with a Gabor analysis (see details in the SI). This single-electron approach has the advantage of being well accepted in the field, and correctly reproduces the spectral properties of resonance-enhanced HHG. However, it remains unclear whether it is sufficient to fully analyze the physical mechanism of the process, especially the time-domain features.

In the second approach, we employed state-of-the-art time-dependent spin density functional theory (TDDFT) [54] using Octopus code [55] (on real-space grids). This approach is

fully *ab-initio* (in 3D) without fitting parameters. Here the ground state of Cr^+ is calculated first with DFT (utilizing the local spin density approximation with an added self-interaction correction,[56] which performs well for HHG[57]). In the ground state, the system is magnetic with half-filled $3d$ orbitals, while all deeper levels are fully occupied (see illustration in Fig. 2(a)). Semi-core $3p$ levels are included in the calculation, while deeper states are treated by norm-conserving pseudopotentials [58]. After obtaining the ground state, the system's response to an ultrashort 800nm laser pulse with similar shape and intensity as in eq.3 is calculated by numerically solving the time-dependent Kohn-Sham (KS) equations of motion:

$$i\partial_t \psi_n^{KS}(\mathbf{r}, t) = \left[-\frac{1}{2}\nabla^2 + v_{KS}(\mathbf{r}) - \mathbf{E}(t) \cdot \mathbf{r} \right] \psi_n^{KS}(\mathbf{r}, t), \quad (3)$$

where n is the orbital index, \mathbf{r} is the electronic coordinate, $\psi_n^{KS}(\mathbf{r}, t)$ are the time-dependent KS orbitals, and v_{KS} is the KS potential which takes the form:

$$v_{KS}(\mathbf{r}, t) = v_{e-ion} + \int d^3r' \frac{n(\mathbf{r}', t)}{|\mathbf{r} - \mathbf{r}'|} + v_{XC}[\rho(\mathbf{r}, t)], \quad (4)$$

with the first term in eq. 4 describes electron-ion interactions (including also interactions with the frozen core states through the pseudopotentials, as well as a self-interaction correction), the second term is the electrostatic Hartree repulsive interaction between electrons, and the last term is the exchange-correlation potential taken in the adiabatic and local spin density approximation with $\rho(\mathbf{r}, t)$ the spin density matrix (from which the electron density $n(\mathbf{r}, t)$ can be obtained). Note that in this notation the orbital index n also refers to spin sub-levels, since up/down spin channels are no longer energy-degenerate (e.g. as a result of spin exchange interactions), though the actual deviations are small.

The TDDFT equations for all initially occupied levels are propagated in real-time (see SI for details), from which we obtain the HHG spectra and time-frequency analysis in a similar manner to the 1D model, but where the emission can be further separated into spin channels (by separating up/down channel contribution to $n(\mathbf{r}, t)$). Time-dependent simulations also include a complex absorbing potential in order to avoid reflections from boundaries.

We employ a third complementary technique where the KS equations are solved numerically by applying the independent particle approximation (IPA), i.e, fixing the KS potential to its form at $t = 0$ with $v_{ks}[\rho(\mathbf{r}, t)] = v_{ks}[\rho(\mathbf{r}, t = 0)]$. In this scheme, the different orbitals

decouple and no longer interact through mean-field terms, but only through the effective potential of the ground-state system. Practically, this removes the contributions of dynamically evolving $e-e$ interactions from the simulations and allows the evaluation of their contribution. We should note that the IPA is usually a very good approximation in strong-field physics; however, it has already been shown to be inadequate in resonance HHG from Ga ions [44], and is generally not expected to hold also in Cr^+ [46, 59].

Importantly, by comparing these three approaches on equal footing we can ascertain the role of interactions, spin, and the atomic-potential landscape on rHHG. All further technical details of these simulations are delegated to the SI.

Acknowledgments. ON gratefully acknowledges the scientific support of Prof. Dr. Angel Rubio. GM acknowledges support from the Israel Science Foundation Grant No. 65618 and Grant No. 89223. AP acknowledges from the Israel Science Foundation Grant No. 1484/24 and the Alon Fellowship of the Israeli Council of Higher Education.

* gilad.marcus@mail.huji.ac.il

† ofern@technion.ac.il

- [1] S. Hädrich, M. Krebs, A. Hoffmann, A. Klenke, J. Rothhardt, J. Limpert, and A. Tünnermann, Exploring new avenues in high repetition rate table-top coherent extreme ultraviolet sources, *Light: Science & Applications* **4**, e320 (2015), publisher: Nature Publishing Group.
- [2] Z. Chang, A. Rundquist, H. Wang, M. M. Murnane, and H. C. Kapteyn, Generation of Coherent Soft X Rays at 2.7 nm Using High Harmonics, *Physical Review Letters* **79**, 2967 (1997), publisher: American Physical Society.
- [3] C. Spielmann, N. H. Burnett, S. Sartania, R. Koppitsch, M. Schnürer, C. Kan, M. Lenzner, P. Wobrauschek, and F. Krausz, Generation of Coherent X-rays in the Water Window Using 5-Femtosecond Laser Pulses, *Science* **278**, 661 (1997), publisher: American Association for the Advancement of Science.
- [4] J. Li, J. Lu, A. Chew, S. Han, J. Li, Y. Wu, H. Wang, S. Ghimire, and Z. Chang, Attosecond science based on high harmonic generation from gases and solids, *Nature Communications* **11**, 2748 (2020), publisher: Nature Publishing Group.

- [5] G. Marcus, W. Helml, X. Gu, Y. Deng, R. Hartmann, T. Kobayashi, L. Strueder, R. Kienberger, and F. Krausz, Subfemtosecond k-Shell Excitation with a Few-Cycle Infrared Laser Field, *Physical Review Letters* **108**, 023201 (2012), publisher: American Physical Society.
- [6] D. Shafir, H. Soifer, B. D. Bruner, M. Dagan, Y. Mairesse, S. Patchkovskii, M. Y. Ivanov, O. Smirnova, and N. Dudovich, Resolving the time when an electron exits a tunnelling barrier, *Nature* **485**, 343 (2012), publisher: Nature Publishing Group.
- [7] O. Smirnova, Y. Mairesse, S. Patchkovskii, N. Dudovich, D. Villeneuve, P. Corkum, and M. Y. Ivanov, High harmonic interferometry of multi-electron dynamics in molecules, *Nature* **460**, 972 (2009), publisher: Nature Publishing Group.
- [8] L. Veisz, D. Rivas, G. Marcus, X. Gu, D. Cardenas, J. Mikhailova, A. Buck, T. Wittmann, C. M. S. Sears, S.-W. Chou, and others, Generation and applications of sub-5-fs multi-10-TW light pulses, in *Conference on Lasers and Electro-Optics/Pacific Rim* (Optical Society of America, 2013) p. TuD2_3, 00005.
- [9] B. Bergues, D. E. Rivas, M. Weidman, A. A. Muschet, W. Helml, A. Guggenmos, V. Pervak, U. Kleineberg, G. Marcus, R. Kienberger, D. Charalambidis, P. Tzallas, H. Schröder, F. Krausz, and L. Veisz, Tabletop nonlinear optics in the 100-eV spectral region, *Optica* **5**, 237 (2018).
- [10] E. Sobolev, M. Volkov, E. Svirplys, J. Thomas, T. Witting, M. J. J. Vrakking, and B. Schütte, Terawatt-level three-stage pulse compression for all-attosecond pump-probe spectroscopy, *Optics Express* **32**, 46251 (2024), publisher: Optica Publishing Group.
- [11] A. Mondal, O. Neufeld, Z. Yin, Z. Nourbakhsh, V. Svoboda, A. Rubio, N. Tancogne-Dejean, and H. J. Wörner, High-harmonic spectroscopy of low-energy electron-scattering dynamics in liquids, *Nature Physics* **19**, 1813 (2023), publisher: Nature Publishing Group.
- [12] Y. Deng, Z. Zeng, P. Komm, Y. Zheng, W. Helml, X. Xie, Z. Filus, M. Dumergue, R. Flender, M. Kurucz, L. Haizer, B. Kiss, S. Kahaly, R. Li, and G. Marcus, Laser-induced inner-shell excitations through direct electron re-collision versus indirect collision, *Optics Express* **28**, 23251 (2020), publisher: Optical Society of America.
- [13] J. Alcalà, U. Bhattacharya, J. Biegert, M. Ciappina, U. Elu, T. Graß, P. T. Grochowski, M. Lewenstein, A. Palau, T. P. H. Sidiropoulos, T. Steinle, and I. Tyulnev, High-harmonic spectroscopy of quantum phase transitions in a high-Tc superconductor, *Proceedings of the*

- National Academy of Sciences **119**, e2207766119 (2022), publisher: Proceedings of the National Academy of Sciences.
- [14] O. Neufeld and O. Cohen, Probing ultrafast electron correlations in high harmonic generation, *Physical Review Research* **2**, 033037 (2020), publisher: American Physical Society.
- [15] O. Neufeld, D. Ayuso, P. Decleva, M. Y. Ivanov, O. Smirnova, and O. Cohen, Ultrasensitive Chiral Spectroscopy by Dynamical Symmetry Breaking in High Harmonic Generation, *Physical Review X* **9**, 031002 (2019), publisher: American Physical Society.
- [16] K. A. Hamer, F. Mauger, A. S. Folorunso, K. Lopata, R. R. Jones, L. F. DiMauro, K. J. Schafer, and M. B. Gaarde, Characterizing particle-like charge-migration dynamics with high-order harmonic sideband spectroscopy, *Physical Review A* **106**, 013103 (2022), publisher: American Physical Society.
- [17] J. Freudenstein, M. Borsch, M. Meierhofer, D. Afanasiev, C. P. Schmid, F. Sandner, M. Liebich, A. Girnguber, M. Knorr, M. Kira, and R. Huber, Attosecond clocking of correlations between Bloch electrons, *Nature* **610**, 290 (2022), publisher: Nature Publishing Group.
- [18] O. Neufeld, J. Zhang, U. De Giovannini, H. Hübener, and A. Rubio, Probing phonon dynamics with multidimensional high harmonic carrier-envelope-phase spectroscopy, *Proceedings of the National Academy of Sciences* **119**, e2204219119 (2022), publisher: Proceedings of the National Academy of Sciences.
- [19] C. Heide, Y. Kobayashi, D. R. Baykusheva, D. Jain, J. A. Sobota, M. Hashimoto, P. S. Kirchmann, S. Oh, T. F. Heinz, D. A. Reis, and S. Ghimire, Probing topological phase transitions using high-harmonic generation, *Nature Photonics* **16**, 620 (2022), publisher: Nature Publishing Group.
- [20] C. P. Schmid, L. Weigl, P. Grössing, V. Junk, C. Gorini, S. Schlauderer, S. Ito, M. Meierhofer, N. Hofmann, D. Afanasiev, J. Crewse, K. A. Kokh, O. E. Tereshchenko, J. Gädde, F. Evers, J. Wilhelm, K. Richter, U. Höfer, and R. Huber, Tunable non-integer high-harmonic generation in a topological insulator, *Nature* **593**, 385 (2021), publisher: Nature Publishing Group.
- [21] J. Zhang, Z. Wang, F. Lengers, D. Wigger, D. E. Reiter, T. Kuhn, H. J. Wörner, and T. T. Luu, High-harmonic spectroscopy probes lattice dynamics, *Nature Photonics* **18**, 792 (2024), publisher: Nature Publishing Group.
- [22] J. L. Krause, K. J. Schafer, and K. C. Kulander, High-order harmonic generation from atoms and ions in the high intensity regime, *Physical Review Letters* **68**, 3535 (1992).

- [23] P. B. Corkum, Plasma perspective on strong field multiphoton ionization, *Physical Review Letters* **71**, 1994 (1993).
- [24] L. He, S. Sun, P. Lan, Y. He, B. Wang, P. Wang, X. Zhu, L. Li, W. Cao, P. Lu, and C. D. Lin, Filming movies of attosecond charge migration in single molecules with high harmonic spectroscopy, *Nature Communications* **13**, 4595 (2022), publisher: Nature Publishing Group.
- [25] D. Baykusheva, M. S. Ahsan, N. Lin, and H. J. Wörner, Bicircular High-Harmonic Spectroscopy Reveals Dynamical Symmetries of Atoms and Molecules, *Physical Review Letters* **116**, 123001 (2016), publisher: American Physical Society.
- [26] E. Frumker, C. T. Hebeisen, N. Kajumba, J. B. Bertrand, H. J. Wörner, M. Spanner, D. M. Villeneuve, A. Naumov, and P. B. Corkum, Oriented Rotational Wave-Packet Dynamics Studies via High Harmonic Generation, *Physical Review Letters* **109**, 113901 (2012), publisher: American Physical Society.
- [27] O. Neufeld, O. Wengrowicz, O. Peleg, A. Rubio, and O. Cohen, Detecting multiple chiral centers in chiral molecules with high harmonic generation, *Optics Express* **30**, 3729 (2022), publisher: Optica Publishing Group.
- [28] N. Saito, P. Xia, F. Lu, T. Kanai, J. Itatani, and N. Ishii, Observation of selection rules for circularly polarized fields in high-harmonic generation from a crystalline solid, *Optica* **4**, 1333 (2017), publisher: Optica Publishing Group.
- [29] O. Neufeld, D. Podolsky, and O. Cohen, Floquet group theory and its application to selection rules in harmonic generation, *Nature Communications* **10**, 405 (2019), publisher: Nature Publishing Group.
- [30] K.-J. Yuan and A. D. Bandrauk, Symmetry in circularly polarized molecular high-order harmonic generation with intense bicircular laser pulses, *Phys. Rev. A* **97**, 023408 (2018).
- [31] R. d. Nalda, E. Heesel, M. Lein, N. Hay, R. Velotta, E. Springate, M. Castillejo, and J. P. Marangos, Role of orbital symmetry in high-order harmonic generation from aligned molecules, *Phys. Rev. A* **69**, 031804 (2004).
- [32] R. Torres, N. Kajumba, J. G. Underwood, J. S. Robinson, S. Baker, J. W. G. Tisch, R. de Nalda, W. A. Bryan, R. Velotta, C. Altucci, I. C. E. Turcu, and J. P. Marangos, Probing Orbital Structure of Polyatomic Molecules by High-Order Harmonic Generation, *Physical Review Letters* **98**, 203007 (2007), publisher: American Physical Society.

- [33] C. B. Madsen and L. B. Madsen, Theoretical studies of high-order harmonic generation: Effects of symmetry, degeneracy, and orientation, *Physical Review A* **76**, 043419 (2007), publisher: American Physical Society.
- [34] M. Suzuki, M. Baba, R. Ganeev, H. Kuroda, and T. Ozaki, Anomalous enhancement of a single high-order harmonic by using a laser-ablation tin plume at 47 nm, *Optics Letters* **31**, 3306 (2006).
- [35] R. A. Ganeev, Generation of high-order harmonics of high-power lasers in plasmas produced under irradiation of solid target surfaces by a prepulse, *Physics-Uspekhi* **52**, 55 (2009).
- [36] N. Rosenthal and G. Marcus, Discriminating between the Role of Phase Matching and that of the Single-Atom Response in Resonance Plasma-Plume High-Order Harmonic Generation, *Physical Review Letters* **115**, 133901 (2015).
- [37] J. T. Costello, E. T. Kennedy, B. F. Sonntag, and C. W. Clark, 3p photoabsorption of free and bound Cr, Cr⁺, Mn, and Mn⁺, *Physical Review A* **43**, 1441 (1991), 00000.
- [38] T. Osawa, K. Kawajiri, N. Suzuki, T. Nagata, Y. Azuma, and F. Koike, Photoion-yield study of the 3p–3d giant resonance excitation region of isolated Cr, Mn and Fe atoms, *Journal of Physics B: Atomic, Molecular and Optical Physics* **45**, 225204 (2012), 00002.
- [39] M. V. Frolov, N. L. Manakov, and A. F. Starace, Potential barrier effects in high-order harmonic generation by transition-metal ions, *Physical Review A* **82**, 023424 (2010), 00037.
- [40] V. Strelkov, Role of Autoionizing State in Resonant High-Order Harmonic Generation and Attosecond Pulse Production, *Physical Review Letters* **104**, 123901 (2010).
- [41] M. Tudorovskaya and M. Lein, High-order harmonic generation in the presence of a resonance, *Physical Review A* **84**, 013430 (2011), publisher: American Physical Society.
- [42] R. A. Ganeev, T. Witting, C. Hutchison, F. Frank, M. Tudorovskaya, M. Lein, W. A. Okell, A. Zaïr, J. P. Marangos, and J. W. G. Tisch, Isolated sub-fs XUV pulse generation in Mn plasma ablation, *Optics Express* **20**, 25239 (2012).
- [43] S. Haessler, V. Strelkov, L. E. Bom, M. Khokhlova, O. Gobert, J.-F. Hergott, F. Lepetit, M. Perdrix, T. Ozaki, and P. Salières, Phase distortions of attosecond pulses produced by resonance-enhanced high harmonic generation, *New Journal of Physics* **15**, 013051 (2013).
- [44] A. A. Romanov, V. V. Strelkov, and A. A. Silaev, Simulation of resonance-enhanced high-order harmonic generation and autoionization decay in Ga⁺ based on time-dependent density-functional theory, *Physical Review A* **110**, 063109 (2024).

- [45] A. A. Romanov, A. A. Silaev, T. S. Sarantseva, M. V. Frolov, and N. V. Vvedenskii, Study of high-order harmonic generation in xenon based on time-dependent density-functional theory, *New Journal of Physics* **23**, 043014 (2021), publisher: IOP Publishing.
- [46] I. S. Wahyutama, T. Sato, and K. L. Ishikawa, Time-dependent multiconfiguration self-consistent-field study on resonantly enhanced high-order harmonic generation from transition-metal elements, *Physical Review A* **99**, 063420 (2019).
- [47] I. Tikhomirov, T. Sato, and K. L. Ishikawa, High-Harmonic Generation Enhanced by Dynamical Electron Correlation, *Physical Review Letters* **118**, 203202 (2017), publisher: American Physical Society.
- [48] N. Moiseyev, *Non-Hermitian Quantum Mechanics* (Cambridge University Press, 2011).
- [49] C. J. Sansonetti and G. Nave, Extended analysis of the spectrum of singly ionized chromium (cr ii), *The Astrophysical Journal Supplement Series* **213**, 28 (2014).
- [50] N. Moiseyev, Quantum theory of resonances: calculating energies, widths and cross-sections by complex scaling, *Physics Reports* **302**, 212 (1998).
- [51] O. Neufeld and O. Cohen, Background-Free Measurement of Ring Currents by Symmetry-Breaking High-Harmonic Spectroscopy, *Physical Review Letters* **123**, 103202 (2019), publisher: American Physical Society.
- [52] S. G. Johnson, Notes on perfectly matched layers (pmls) (2021), arXiv:2108.05348 [cs.CE].
- [53] M. R. Miller, (2016), *Time Resolving Electron Dynamics in Atomic and Molecular Systems Using High-Harmonic Spectroscopy*, Ph.D. thesis, University of Colorado Boulder.
- [54] M. a. L. Marques and E. K. U. Gross, Time-dependent density functional theory, *Annual Review of Physical Chemistry* **55**, 427 (2004), publisher: Annual Reviews.
- [55] N. Tancogne-Dejean, M. J. T. Oliveira, X. Andrade, H. Appel, C. H. Borca, G. Le Breton, F. Buchholz, A. Castro, S. Corni, A. A. Correa, U. De Giovannini, A. Delgado, F. G. Eich, J. Flick, G. Gil, A. Gomez, N. Helbig, H. Hübener, R. Jestädt, J. Jornet-Somoza, A. H. Larsen, I. V. Lebedeva, M. Lüders, M. A. L. Marques, S. T. Ohlmann, S. Pipolo, M. Rampp, C. A. Rozzi, D. A. Strubbe, S. A. Sato, C. Schäfer, I. Theophilou, A. Welden, and A. Rubio, Octopus, a computational framework for exploring light-driven phenomena and quantum dynamics in extended and finite systems, *The Journal of Chemical Physics* **152**, 124119 (2020).
- [56] C. Legrand, E. Suraud, and P.-G. Reinhard, Comparison of self-interaction-corrections for metal clusters, *Journal of Physics B: Atomic, Molecular and Optical Physics* **35**, 1115 (2002).

- [57] O. Neufeld, N. Tancogne-Dejean, and A. Rubio, Benchmarking Functionals for Strong-Field Light-Matter Interactions in Adiabatic Time-Dependent Density Functional Theory, *The Journal of Physical Chemistry Letters* **15**, 7254 (2024), publisher: American Chemical Society.
- [58] C. Hartwigsen, S. Goedecker, and J. Hutter, Relativistic separable dual-space Gaussian pseudopotentials from H to Rn, *Physical Review B* **58**, 3641 (1998), publisher: American Physical Society.
- [59] A. W. Bray, D. Freeman, F. Naseem, V. K. Dolmatov, and A. S. Kheifets, Correlation-enhanced high-order-harmonic-generation spectra of Mn and Mn +, *Physical Review A* **101**, 053415 (2020).

Supplementary Information for
“Correlation-induced phase shifts and time delays in resonance
enhanced high harmonic generation from Cr⁺”

ADDITIONAL TECHNICAL DETAILS

1D model

The 1D potential

To construct a rounded potential, we first defined the function:

$$u(x; l) = \frac{\tanh\left(\alpha\left(x - \frac{l}{2}\right)\right) - \tanh\left(\alpha\left(x + \frac{l}{2}\right)\right)}{2} \quad (1)$$

which constitutes a rounded analogue of the function $-\text{rect}\left(\frac{x}{l}\right)$. Here, the parameter α controls the degree of smoothing:

$$\lim_{\alpha \rightarrow \infty} u(x; l) = -\text{rect}\left(\frac{x}{l}\right) \quad (2)$$

This function served as a building block for the barriers and the well:

$$V(x) = \underbrace{V_w u(x; l_w)}_{\text{well}} + V_b \underbrace{\left[u\left(x + \frac{l_w}{2}; l_b\right) + u\left(x - \frac{l_w}{2}; l_b\right) \right]}_{\text{barriers}} \quad (3)$$

Hamiltonian Construction

The one dimensional (1D) model Hamiltonian was constructed on a real-space grid with the kinetic energy term represented using a second-order central-difference approximation for the second derivative. The box size was chosen as $L = 100$ (a.u.), with step size $\Delta x = 0.28$ (a.u.). The main potential parameters discussed in the main text define the well-barrier system and resulting resonance state: well-depth V_w , well width l_w , barrier height V_b , and barrier width l_b . The resonance energy was tuned by varying each of the four parameters of the potential (calculations discussed below). For all the 1D simulations we chose the following values (in [a.u.]: $l_w = 1.7$; $V_w = -1.4$; $V_b = 1.5$; $\alpha = 8$. For our main simulation, with an MS lifetime of $0.17T$, we chose $l_b = 2$.

For time-dependent simulations the TDSE was solved with a variable time step using MATLAB's [1] native ode45 solver, and with a laser wavelength of $\lambda = 800$ nm and a typical laser power of 3.51×10^{14} W/cm², and pulse duration of 21.23 fs full width half max

(FWHM). Under these parameters the resonant enhancement arises in the 29th harmonic. To prevent reflections from the boundaries of the box, we employed the method of perfectly matched layers (PML) [2]. The width of the PML was set to one-fifth of the box size on each side.

Complex-Scaling

To study the resonance enhancement of HHG, knowledge and control of the energy and life-time of the meta-stable state are crucial. For a given potential exhibiting a shape-resonance, this information can be numerically calculated by means of the complex-scaling method [3].

In complex scaling, the position operator undergoes an analytical continuation defined as $\hat{X}(\theta) = e^{i\theta} \hat{X}$. Consequently, the momentum operator scales as $\hat{P}(\theta) = e^{-i\theta} \hat{P}$, leading to the following scaling of the Hamiltonian: $\hat{H}(\theta) = \frac{e^{-2i\theta} \hat{P}^2}{2} + V(e^{i\theta} \hat{X})$. It has been demonstrated [4] that the negative eigenvalues of the Hamiltonian, corresponding to bound-state energies, remain unchanged under this transformation. In contrast, the continuum-state energies scale as $E(\theta) = |E|e^{-2i\theta}$. For meta-stable states, commonly referred to as resonances, a critical angle θ_c exists. Beyond this angle the resonance energies cease to rotate, and assume to complex value $E(\theta_c) = \epsilon - i\Gamma$, where ϵ represents the resonance peak center, and Γ denotes its width.

HHG Calculation

The HHG spectrum was calculated by taking the Fourier transform of the dipole acceleration, which was derived using Ehrenfest theorem [5]

$$\begin{aligned} \ddot{d}(t) &= \frac{d}{dt} \langle \hat{P} \rangle = - \left\langle \frac{\partial}{\partial x} V(x, t) \right\rangle \\ &= - \int_{-L/2}^{L/2} \psi^*(x, t) \frac{\partial}{\partial x} V(x, t) \psi(x, t) dx \end{aligned} \quad (4)$$

where $V(x, t)$ represents the sum of the atomic potential and the laser potential. The dipole acceleration was multiplied by a Blackman filter, and then zero padded on either side with 4 times the signal length, prior to taking the Fourier transform. To evaluate the Fourier transform we integrated over the entire zero-padded signal, using MATLAB's [1] fft. The Gabor transform was calculated by taking the Fourier transform of the dipole acceleration multiplied by a moving Gaussian window. The width of the window, defined by 1 standard

deviation, was set to $\frac{1}{35}$ of the laser period, with an overlap of 95% between each iteration.

$$GT(\tau) = \int_0^{t_{fin}} \ddot{d} e^{-\frac{1}{2}\left(\frac{t-\tau}{\Delta t}\right)^2} e^{-i\omega t} dt \quad (5)$$

This provides a way to analyze the spectral composition within a specific temporal window, independently of the remainder of the signal. By examining the dipole oscillations in this manner, we obtain the spectrum as a function of time. In the context of HHG, this reflects the recombination times of the different trajectories, each emitting radiation according to its kinetic energy.

Group Delay Correction

The group delay (GD) of a pulse is defined as [6]:

$$\tau_g(\omega) = -\frac{\partial\phi(\omega)}{\partial\omega} \quad (6)$$

Note that here ω is treated as an independent variable, in contrast to eq. 13, where ω denotes the driving frequency. If a constant group delay τ_0 is introduced, the phase is modified as:

$$\tilde{\phi} = \phi - \omega\tau_0 \quad (7)$$

such that

$$\begin{aligned} \tilde{\tau} &= -\frac{\partial\tilde{\phi}(\omega)}{\partial\omega} \\ &= -\frac{\partial\phi(\omega)}{\partial\omega} + \tau_0 \\ &= \tau_g + \tau_0 \end{aligned} \quad (8)$$

This is tantamount to a temporal shift, as would occur when traversing a material with a linear dispersion. This is evident from the shift property of the Fourier transform:

$$\mathcal{F}[E(t - \tau_0)] = \left| \tilde{E}(\omega) \right| e^{i(\phi(\omega) - \omega\tau_0)} \quad (9)$$

We may consider the group delay of an attosecond pulse, where the phases are extracted via a RABBIT measurement, as given by eq. 23. A temporal shift τ_0 between the laser and the signal results in a corresponding shift in the argument of the SB cosine function from eq. 20:

$$2\omega(\tau - \tau_0) + \Phi \quad (10)$$

Note that in eq. 23 ω refers to the driving frequency, whereas in the above discussion ω denotes the frequency as an independent variable in the spectral domain. The above may be written as:

$$2\omega\tau + \tilde{\Phi} \quad (11)$$

with $\tilde{\Phi}$ equal to:

$$\tilde{\Phi} = \Phi - 2\omega\tau_0 \quad (12)$$

In Fig. 4 (a) the harmonic phases due to the different models are compared. The 1D results (blue curve) shows the 1D phases with an addition of a constant group delay. We found a group delay of $-\frac{T}{8}$ aligns the 1D curve with that of the IPA model (orange curve). This is equivalent to an increase of $\frac{\pi}{4}$ between two adjacent (odd) harmonics.

TDDFT simulations

This section describes additional technical details about the DFT and TDDFT simulations employed throughout the main text. All DFT and TDDFT simulations were performed within Octopus code on a real-space grid, where the grid spacing was taken as 0.35 Bohr, and the grid was cartesian with spherical boundaries with a radius of 45 Bohr. Ground state simulations within spin DFT were first performed to obtain the initial KS orbitals (at $t = 0$), where we employed the local density approximation with an added self-interaction correction as discussed in the main text. These states were then propagated within TDDFT using a time step of 2.9 attoseconds. At each time step we computed the induced dipole moment in the system (separated to spin-up and down channels), from which we numerically obtained the dipole acceleration and corresponding HHG spectra as described in the main text, but directly from the calculated dipoles (instead of employing Ehrenfest theorem), and where HHG spectra were also filtered with a temporal gaussian window. During propagation, we added a complex absorbing potential along the boundaries of width 15 Bohr to avoid reflections.

IPA simulations were performed within the same methodology, except that the KS potential was frozen to its form at $t = 0$, as discussed in the main text.

Absorption and photoionization cross-section simulations presented in this SI were performed in a similar strategy, but by varying the driving laser wavelength and calculating: (i) The induced response at the driving wavelength (absorption), (ii) the total photo-ionization yield obtained via the portion of the electron density that was absorbed at the boundaries at the end of the simulation.

Gabor transforms were calculated similarly to the 1D model with a gaussian window function with a width of a third of an optical period.

RABBIT ANALYSIS

We performed a RABBIT-like calculation where the signal is expressed as:

$$S = \left\{ \mathcal{F} \left[\left| \ddot{d}(t) + \cos(\omega(t - \tau)) \right|^2 \right] \right\}^2 \quad (13)$$

where \ddot{d} represents the second time derivative of the dipole moment's expectation value, and τ denotes the time delay between the local oscillator $\cos(\omega t)$ and $\ddot{d}(t)$. To demonstrate that this indeed retrieves the RABBIT spectrum, we first evaluate the argument of the Fourier transform:

$$I(t; \tau) = \left| \ddot{d}(t) + \cos(\omega(t - \tau)) \right|^2 \quad (14)$$

We may approximate the harmonic emission by the sum:

$$\ddot{d}(t) = \sum_{q \in \text{odd}} c_q \cos(q\omega t + \phi_q) \quad (15)$$

where ϕ_q is the harmonic phase. Substituting this sum into eq. 14 we get:

$$I(t; \tau) = \left| \sum_{q \in \text{odd}} c_q \cos(q\omega t + \phi_q) + \cos(\omega(t - \tau)) \right|^2 \quad (16)$$

The expansion of the square in the above expression includes the following terms:

$$I \propto 2(c_q \cos(q\omega t + \phi_q) \cos(\omega(t - \tau)) + c_{q+2} \cos((q+2)\omega t + \phi_{q+2}) \cos(\omega(t - \tau))) \quad (17)$$

Using the cosine sum-angle formula the above products simplify to the following sums:

$$\begin{aligned} I \propto & 2c_q [\cos((q+1)\omega t - \omega\tau + \phi_q) + \cos((q-1)\omega t + \omega\tau + \phi_q)] \\ & + 2c_{q+2} [\cos((q+3)\omega t - \omega\tau + \phi_{q+2}) + \cos((q+1)\omega t + \omega\tau + \phi_{q+2})] \end{aligned} \quad (18)$$

Since we are interested in the SB, we further investigate the terms with frequency $(q+1)\omega$:

$$\begin{aligned} I_{q+1} &= 2[c_q \cos((q+1)\omega t - \omega\tau + \phi_q) + c_{q+2} \cos((q+1)\omega t + \omega\tau + \phi_{q+2})] \\ &= e^{i(q+1)\omega t} (c_q e^{i(-\omega\tau + \phi_q)} + c_{q+2} e^{i(\omega\tau + \phi_{q+2})}) + c.c. \end{aligned} \quad (19)$$

Lastly, we evaluate the Fourier transform of eq.19 to obtain the $(q+1)^{th}$ SB:

$$\begin{aligned} \left| \tilde{F}((q+1)\omega) \right|^2 &\propto |c_q e^{i(-\omega\tau + \phi_q)} + c_{q+2} e^{i(\omega\tau + \phi_{q+2})}|^2 \\ &= c_q^2 + c_{q+2}^2 + 2c_q c_{q+2} \cos(2\omega\tau + \Phi_{q+1}) \end{aligned} \quad (20)$$

where the SB phase Φ is equal to:

$$\begin{aligned}
\Phi_2 &= \phi_3 - \phi_1 \\
\Phi_4 &= \phi_5 - \phi_3 \\
\Phi_6 &= \phi_7 - \phi_5 \\
&\vdots \\
\Phi_{q+1} &= \phi_{q+2} - \phi_q
\end{aligned} \tag{21}$$

The sideband signal (eq. 20) oscillates as a function of delay τ with frequency 2ω , and has a phase equal to the difference between the phases of two adjacent harmonics. By summing over the SB phases we obtain the harmonic phase, up to a global phase:

$$\begin{aligned}
\Phi_2 + \Phi_4 &= \cancel{\phi_3} - \phi_1 + \phi_5 - \cancel{\phi_3} = \phi_5 - \phi_1 \\
\Phi_2 + \Phi_4 + \Phi_6 &= \cancel{\phi_5} - \phi_1 + \phi_7 - \cancel{\phi_5} = \phi_7 - \phi_1
\end{aligned} \tag{22}$$

The q^{th} harmonic phase is equal to:

$$\phi_q = \phi_1 + \sum_{m \in \text{even}}^{m=q-1} \Phi_m \tag{23}$$

The visibility of the SB is determined by:

$$V = \frac{2c_q c_{q+2}}{c_q^2 + c_{q+2}^2} \tag{24}$$

The calculated visibility referred to in Fig.4 (b-c) is calculated by the above expression, where the values of the coefficients c_q are obtained from the harmonic spectra. To determine the visibility of the RABBIT interferogram i.e. the 'observed' data, we fitted a cosine function with a DC offset to each SB and calculated the ration between the oscillation amplitude with the DC amplitude, in accordance with the definition in eq. 24.

COMPLEMENTARY RESULTS

1D model HHG dependence on barrier width

The lifetime of the MS increases with both the barrier width and height [7, 8]. As the barrier becomes wider, the MS wavefunction becomes more localized within the potential well, increasing the lifetime. To examine how this influences rHHG, we repeated our simulation, sweeping over width ranging from 1.5 to 2.5 a.u. This corresponds to lifetime values ranging

from $0.072T$ to $0.25T$. We present the spectra obtained from these simulations in Fig. 1 (a).

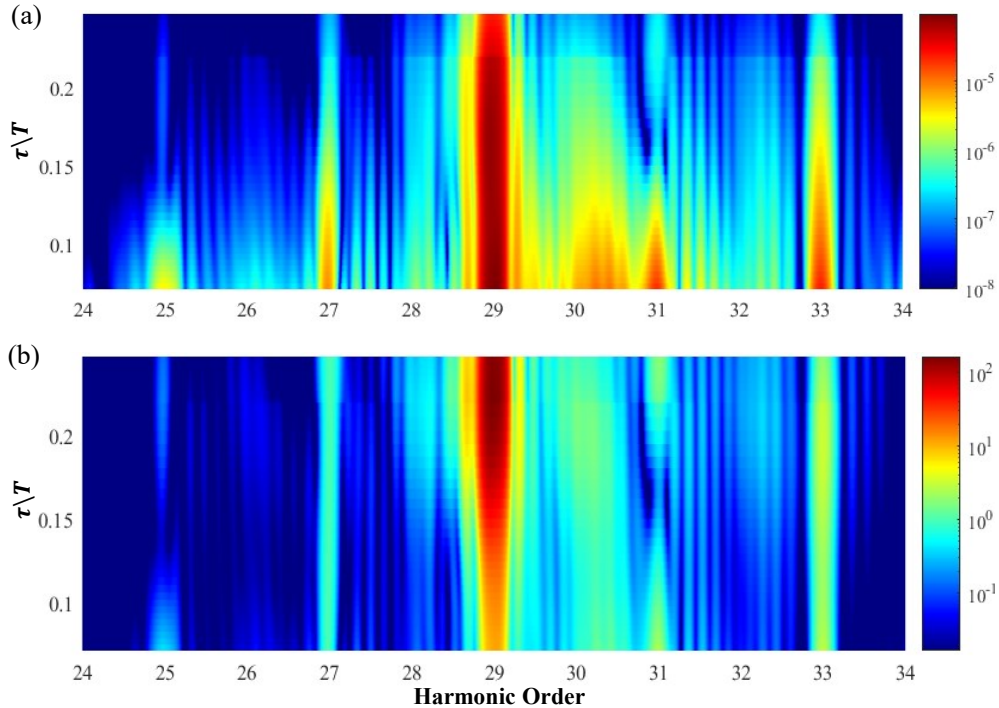


Figure 1. Harmonic spectra for varying MS lifetimes. The lifetimes are normalized by the driving period. **(a)** A clear resonance enhancement is observed at H29. The harmonic yield decreases across all harmonic orders as the MS lifetime increases, though this decrease is less pronounced for H29. **(b)** The same spectra, normalized to the intensity of H27. The intensity of H29 represents the enhancement factor, which increases with MS lifetime.

A clear resonance enhancement is observed at H29. The yield of non-resonant harmonics generally decreases as the lifetime increases. This trend is consistent with a recollision-based model as discussed in the main text. Although the yield of the resonant harmonic also decreases, it does so to a lesser extent. In 1 (b) the same spectra are shown but normalized to the intensity of H27, such that the intensity of H29 reflects the enhancement factor (I_{29}/I_{27}). As the lifetime increases, the enhancement factor also increases.

1D model HHG dependence on PML position

In our 1D simulation, we employed a PML (Perfectly Matched Layer) at the boundaries of the simulation domain to suppress reflections. The PML also served as a diagnostic tool to test whether H29 is emitted through tunnel ionization followed by recombination. By extending the absorbing region inward from the boundaries, we could selectively suppress the long trajectories associated with HHG. Fig. 2 shows the Gabor transform and corresponding spectra for two different PML widths. In the top panel (a), the PML extends 10 a.u. into the simulation domain, remaining well outside the region reached by the calculated electron

trajectories corresponding to the cutoff energy. The bottom panel (b) presents the results with a PML width of 30 a.u. which extends well beyond the range of the long trajectories associated with H29. As expected, these trajectories are clearly suppressed in the Gabor transform and the corresponding harmonics. Most notably, H29 exhibits a marked decrease in intensity in the spectrum. The suppression of the long trajectories is also evident by

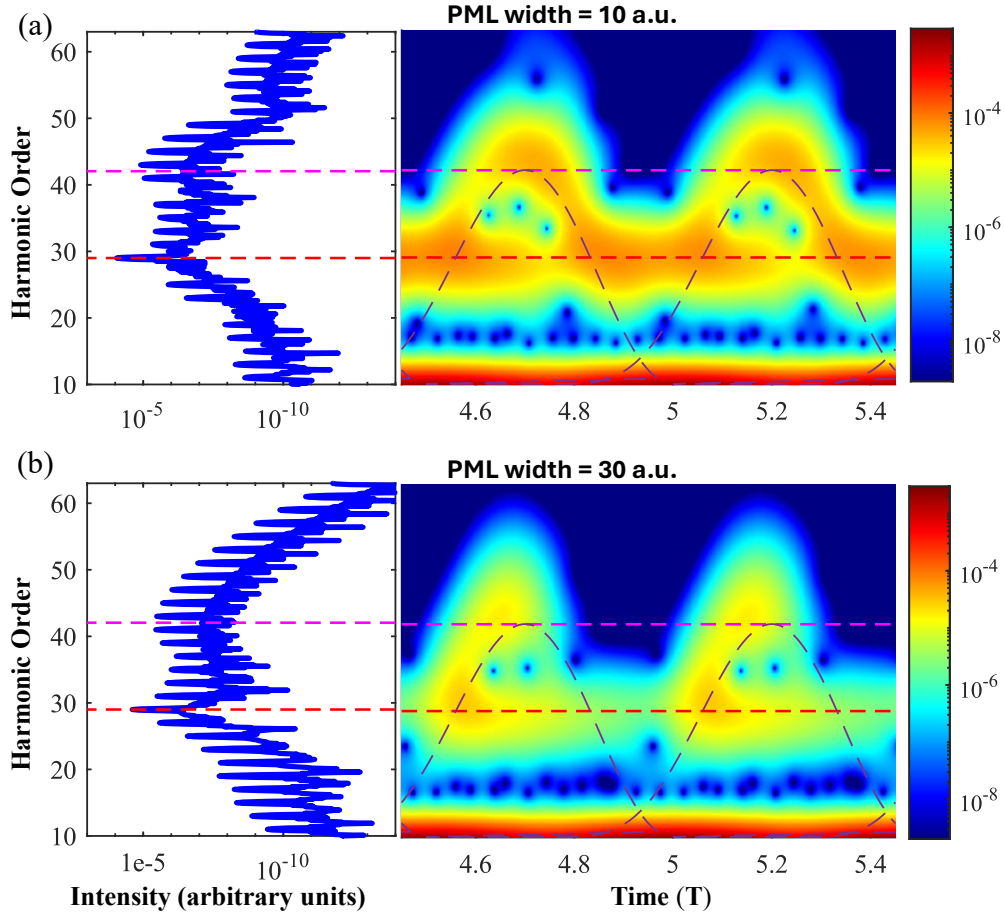


Figure 2. Gabor transform (right) and corresponding spectra (left) for different PML width. The PML is positioned at the boundary of the simulation domain, and extends inwards towards the center. **(a)** PML width of 10 a.u. Both long and short trajectories are clearly visible in the Gabor transform. **(b)** PML width of 30 a.u. The long trajectories are suppressed, diminishing the intensities of the highest harmonics, including H29.

examining the wavefunction directly, as shown in Fig. 3, where $|\psi(x, t)|^2$ is plotted. In the top panel (a), with a PML width of 10 a.u., the absorption of the wavefunction is clearly visible at the boundaries of the box, where only open trajectories of non-returning electrons are absorbed. In the bottom panel (b), where the PML extends 30 a.u. units inward, the long trajectories are absorbed, preventing recombination.

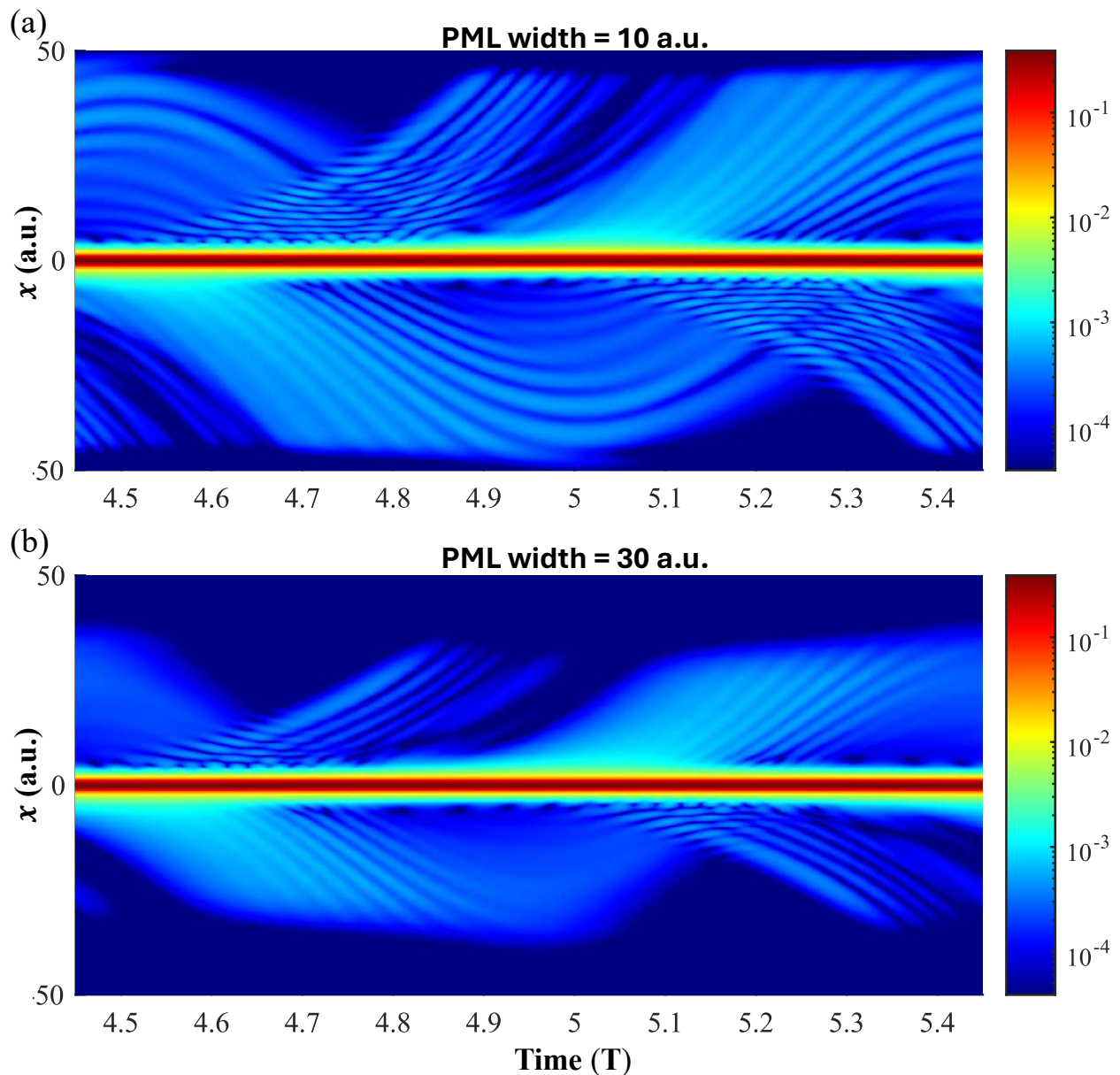


Figure 3. Plot of $|\psi(x, t)|^2$ for different values of PML width. The PML is positioned at the box boundary, and extends inward. **(a)** PML width of 10 a.u. Absorption of the wavefunction occurs at the boundaries of the simulation box, where only open trajectories of non-returning electrons are absorbed. **(b)** PML width of 30 a.u. The long trajectories are absorbed, preventing recombination

TDDFT absorption/photoemission calculations

We further present here complementary absorption and photoionization cross-section calculations performed within TDDFT and the IPA. Fig. 4 presents the key results, showing that single-photon absorption at the resonance wavelength is dominated by the spin-down channel (i.e. $3p$ down states), which only arises when electronic correlations are considered. In other words, in the IPA there is no resonant absorption peak at the resonance energy, pre-

venting a strong transition of $3p$ levels into the AIS (the overall enhancement in absorption with correlations included in the simulations is $\sim 1000\%$). Contrarily, photoionization cross section at the resonance are dominated by the spin-up electron channel (i.e. $3d$ up states), as expected from their lower ionization potential. Notably, there is also a substantial enhancement of photoemission from the $3d$ up states if correlations are included in the simulation (about 50% enhancement), though not resonantly a very sharp enhancement as expected if resonance states are involved. This could indicate a more intricate channel by which the $3d$ photoionization enhancement is still mediated by the resonance through interaction with the $3p$ down electrons, supporting our interpretation in the main text for the enhancement mechanism.

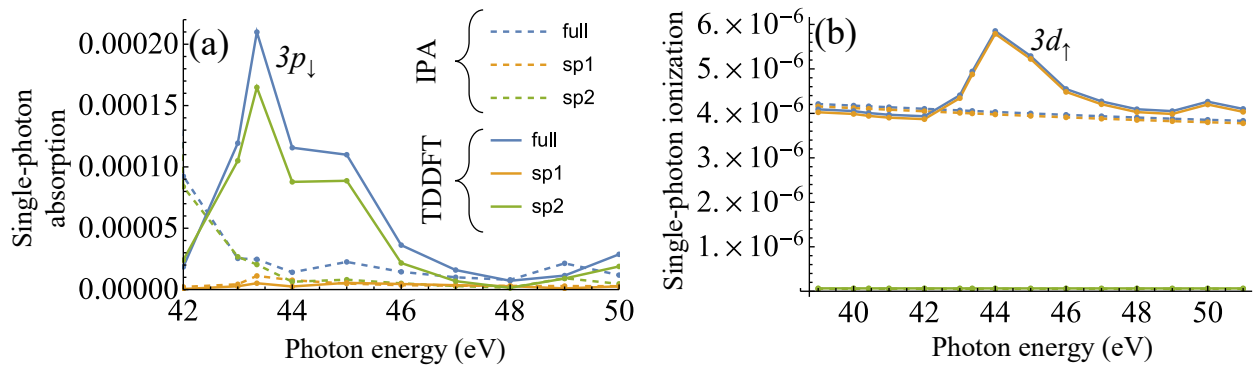


Figure 4. Single-photon absorption and ionization spectra in Cr^+ calculated within TDDFT and the IPA around the resonance, separated to spin channel contributions

-
- [1] The MathWorks Inc., matlab version: 23.2.0.2485118 (r2023b) update 6, <https://www.mathworks.com> (2023).
 - [2] S. G. Johnson, Notes on perfectly matched layers (pmls) (2021), arXiv:2108.05348 [cs.CE].
 - [3] N. Moiseyev, Quantum theory of resonances: calculating energies, widths and cross-sections by complex scaling, *Physics Reports* **302**, 212 (1998).
 - [4] J. Aguilar and J. M. Combes, A class of analytic perturbations for one-body Schrödinger Hamiltonians, *Communications in Mathematical Physics* **22**, 269 (1971).
 - [5] M. R. Miller, (2016), Time Resolving Electron Dynamics in Atomic and Molecular Systems Using High-Harmonic Spectroscopy, Ph.D. thesis, University of Colorado Boulder.
 - [6] A. M. Weiner, Ultrafast optics (John Wiley & Sons, 2011).
 - [7] R. Zavin and N. Moiseyev, One-dimensional symmetric rectangular well: from bound to resonance via self-orthogonal virtual state, *Journal of Physics A: Mathematical and General* **37**, 4619 (2004).
 - [8] H. M. Nussenzveig, The poles of the S-matrix of a rectangular potential well of barrier, *Nuclear Physics* **11**, 499 (1959).